PHOTONICS Research

Highly efficient achromatic subdiffraction focusing lens in the near field with large numerical aperture

Jin Chen,[1] Hongchen Chu,[2] Yun Lai,[2] Huanyang Chen,[3] Weili Song,[1,4] Mingji Chen,[1,*] and Daining Fang[1,5]

[1]Institute of Advanced Structure Technology, Beijing Institute of Technology, Beijing 100081, China
[2]National Laboratory of Solid State Microstructures, School of Physics, Nanjing University, Nanjing 210093, China
[3]Institute of Electromagnetics and Acoustics and Department of Physics, Xiamen University, Xiamen 361005, China
[4]e-mail: weilis@bit.edu.cn
[5]e-mail: fangdn@bit.edu.cn
*Corresponding author: mjchen81@bit.edu.cn

Received 12 April 2021; revised 3 August 2021; accepted 20 August 2021; posted 24 August 2021 (Doc. ID 427322); published 30 September 2021

The achromatic subdiffraction lens with large numerical aperture (NA) is of significant importance in optical imaging, photolithography, spectroscopy, and nanophotonics. However, most of the previous research on subdiffraction lenses has been restricted by limited bandwidth and efficiency as well as severe chromatic aberrations. In this paper, a semicircular gradient index lens (sGRIN) with a modified refractive index profile originated from a Maxwell fish-eye lens is put forward to achieve highly efficient (above 81%) achromatic (4–20 GHz) subdiffraction focusing at the focusing line (around 0.28λ) with large NA of 1.3 and broadband diffraction-limited far-field radiation (4–16 GHz) theoretically, which overcomes the drawbacks of previous works. The presented lens is designed by gradient dielectric metamaterials. Evanescent waves ignited at the lens/air interface and transformation of electromagnetic (EM) waves with high spatial frequency in sGRIN to EM waves with low spatial frequency in air are responsible for subdiffraction focusing and diffraction-limited far-field radiation, respectively. Experimental results demonstrate the excellent performance of achromatic subdiffraction focusing and diffraction-limited far-field radiation. The presented lens has great potential to be applied in subdiffraction imaging systems.

https://doi.org/10.1364/PRJ.427322

1. INTRODUCTION

Controlling the propagation of electromagnetic (EM) waves in a predesigned way is highly expected due to curiosity in fundamental physics and increasing technological demands in imaging and telecommunications. The bulky dielectric refractive lenses and parabolic mirrors are conventional lenses for focusing and imaging. The resolution of conventional lenses is confined to $0.5\lambda/\mathrm{NA}$ due to the decadence of evanescent waves, where NA is the lens numerical aperture. To overcome the resolution of conventional lenses restricted by the diffraction limit [1], a large number of approaches have been put forward to accomplish superresolution, owing to its paramount importance in various applications such as imaging, noncontact sensing, and photolithography. A perfect lens originating from a flat lens comprising ideal negative refraction medium, was first pushed forward [2] to fulfill a perfect image via restoring both the phase of propagating waves and the amplitude of evanescent states. Various superlenses were later fabricated to achieve negative refraction and were experimentally verified through different ways such as a thin slab of silver [3] or SiC [4], photonic crystals [5], negative-index metamaterial [6] and metal–dielectric composites [7]. However, for these resonance-based negative index designs, the loss of materials made it inevitable that superlenses only illustrate subwavelength performance in the near field [8]. Alternatively, hyperlenses were proposed, relying on strongly anisotropic metamaterials with hyperbolic dispersions [9,10] to construct high-resolution imaging in the far field by magnifying deep subwavelength detail of objects. 2D and 3D versions of hyperlenses [11–13] were implemented by curved multilayer structures with alternatively arranged metal and dielectric layers. But the inherent loss and narrowband characteristics of superlenses and hyperlenses greatly hinder their applications.

To solve the intrinsic problem of superlenses and hyperlenses, the superoscillation lens (SOL) has been proposed. Based on the mechanism of superoscillation [14–17], many sca-

lar SOLs [18–20] and vector SOLs [21–23] have been designed to accomplish far-field superresolution without evanescent waves. However, these SOLs' working bandwidth is restricted to just one single frequency [24] or some discrete frequency points [25]. Even worse, when the resolution increases, the sidelobe of the focusing spot in the far field will dramatically rise [26]. To overcome the drawbacks of SOL, supercritical lenses (SCLs) [27,28] and photon sieves [29] were proposed. Ultralong working distance and subdiffraction focusing (0.407λ) without significant sidelobes were achieved by SCLs. But the problem of narrow operational bandwidth was not solved. On the other hand, achromatic metalenses originating from metasurface [30–32] that have gained broad bandwidth and outstanding imaging performance in the visible [33–35] and terahertz regime [36] as well as the near-infrared spectrum [37,38] are confined by the Abbe diffraction limit and limited NA. The solid immersion lens [39], a thick lens on the microscale [40] and nanoscale [41] has both a higher magnification and NA due to application of high refractive index (RI) solid material and suffers from strong chromatic aberrations. Until now, it has still been a great challenge to implement highly efficient achromatic subdiffraction lenses with large NAs.

Moreover, gradient refractive index (GRIN) lenses have presented excellent performance in focusing [42–46], imaging [47–49], magnifying the far field [50,51], and beam forming [52,53]. The Maxwell fish-eye (MFE) lens [54] has been validated to generate an achromatic image with a large NA. Consequently, a new semicircular gradient index lens (sGRIN) with a modified RI distribution is proposed. Broadband (7–13 GHz) highly efficient (above 89%) achromatic subdiffraction focusing at the focusing line with full width at half-maximum (FWHM) around 0.28λ and NA of 1.3 as well as diffraction-limited far-field radiation (0.56λ) from 4 to 16 GHz has been realized experimentally. Composite dielectric materials and photocurable resin with low loss have been used to design and fabricate a multilayered gradient periodic structure. Both theoretical analysis and measured data reveal that the presented lens displays quite good performance in subdiffraction focusing and diffraction-limited radiation over a broadband of frequencies. This sGRIN's verified ability to generate achromatic subdiffraction focusing with a large NA and diffraction-limited far-field radiation indicates that it could be integrated into subdiffraction imaging systems.

2. THEORETICAL DESIGN OF sGRIN

Let us start from the RI profile of the classical half-MFE lens as follows:

$$n(r) = \begin{cases} \frac{2n_0}{1+(r/R)^2} & 0 < r < R \\ 1 & r \geq R \end{cases}, \tag{1}$$

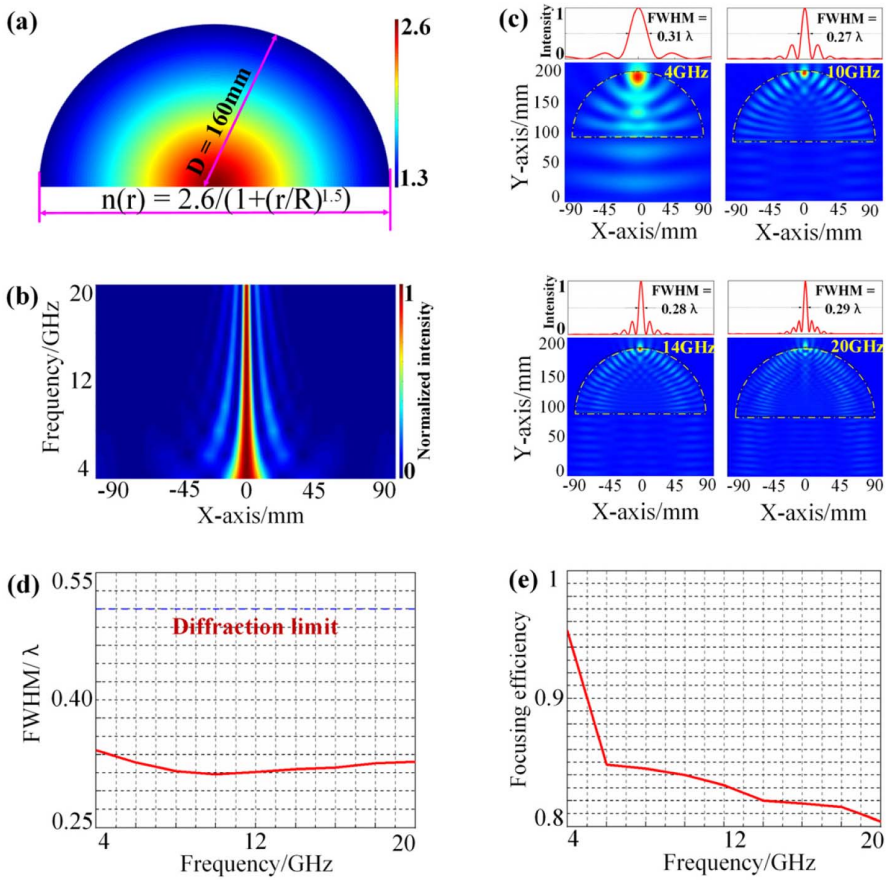

Fig. 1. Focusing performance of sGRIN. (a) RI profile of sGRIN; (b) map of electric near-field intensity profile at the focusing line in the frequency range of 4 to 20 GHz; (c) calculated electric near-field intensity distribution; (d) related FWHM; (e) focusing efficiency of proposed sGRIN.

where R defines the radius of the lens, r is the distance from the center of the lens, and n_0 indicates the RI at the circumstance.

n_0 is conventionally determined as 1; such a half-MFE lens is impedance matching to the background medium (usually free space). There are no reflection and evanescent waves arising at the lens/air interface. The FWHM and NA of this classical half-MFE lens are around 0.36λ and 1.0, respectively. In order to arouse evanescent waves at the upper side of lens/air interface to further enhance the focusing performance and achieve broadband achromatic subdiffraction focusing, the value of n_0, which is also the RI at the lens/air interface, should be increased. However, the RI at the edge must be reasonable because a too large RI at the lens/air interface will lead to severe impedance mismatch. Then, the achromatic focusing performance will also severely deteriorate. According to this principle, through a large number of parametric simulations in exhaustive methods via the commercial software package COMSOL 5.5, it is found that the value of n_0 should be increased slightly to 1.3. From full-wave numerical simulations, it can be seen that the related FWHM of the focusing spot descends to around 0.28λ, which has overcome the diffraction limit further compared to the classical half-MFE lens. The proposed sGRIN is achromatic, and the corresponding half of the light cone angle is 90°, as displayed in Fig. 1(c). In this specific design, the related NA of presented sGRIN could be as large as 1.3.

For obtaining the lowest reflection at the lower side of the lens/air interface and widest operating frequency band, through numerous numerical simulations via the exhaustive method for the n_0 of 1.3 in COMSOL 5.5, it is found that the RI distribution of the lens should be adjusted to $2.6/[1 + (r/R)^{1.5}]$, as depicted in Fig. 1(a). To study the subdiffraction focusing of the designed lens quantitatively, the map of near-field electric intensity distribution at the focusing line from 4 to 20 GHz is shown in Fig. 1(b). The higher the frequency is, the narrower the focusing band is. The related near-field electric intensity profile and FWHM are illustrated in Figs. 1(c) and 1(d). The values of FWHM are all around 0.30λ, as shown in Fig. 1(d). To evaluate focusing efficiency, the focusing efficiency defined by the fraction of collected light at the focus line with a radius equal to 3 times the FWHM of the focus spot [55] is adopted. Figure 1(e) reveals focusing efficiency at the focusing line is all above 81% numerically for this continual model. Achromatic subdiffraction focusing originating from evanescent waves at the upper side of the lens/air interface is verified, as predicted.

According to the reciprocity principle [56], the process of transforming EM wave propagation with low spatial frequency in air into EM wave propagation with high spatial frequency in sGRIN to generate subdiffraction focusing [Fig. 1(c)] can be reversed. This is confirmed by applying the two-point sources technique, which has been widely adopted to determine the resolution of an optical system. Two-point sources are located at the vertex of the sGRIN separated by 0.56λ (10 GHz). It can be seen from Fig. 2(b) that an EM wave with high spatial frequency experiences strong interaction with the designed GRIN lens, which arouses effective propagation. The electric field received at the far field ($y > 3\lambda$) is about $|E| \sim 0.4$. Since source

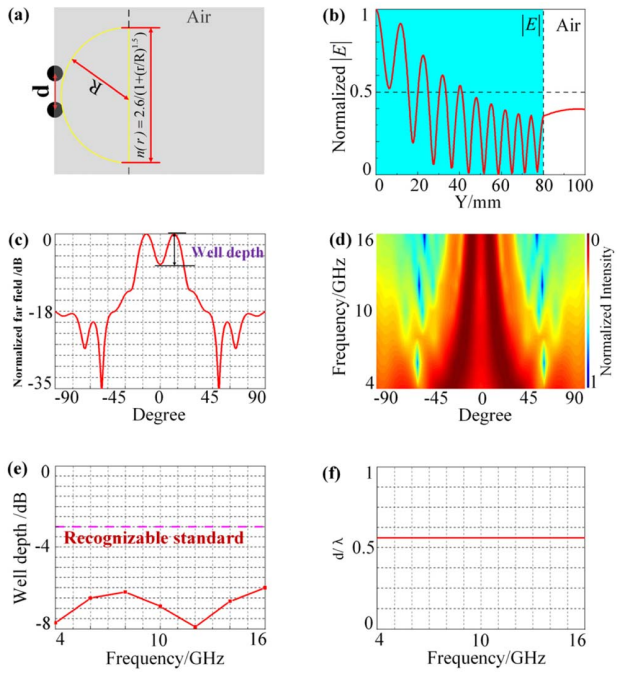

Fig. 2. Principle of diffraction-limited far-field radiation of sGRIN. (a) sGRIN with RI distribution of $2.6/[1 + (r/R)^{1.5}]$; (b) mean electric field amplitude as a function of distance from two-point sources (transverse electric polarization), EM waves experience strong interaction with gSIL and transport into the far field. Gradient periodic modulation in sGRIN is observed. (c) Far-field radiation pattern of two-point sources of 10 GHz; (d) map of normalized far-field intensity profile of two-point sources with distances of 0.56λ from 4 to 16 GHz; (e) related well depth; and (f) the distance between the two sources.

amplitude $|E| = 1$, this equals $|E|^2 = 16\%$ of total EM energy, which demonstrates that near-field subwavelength information is transported to the far field. Therefore, EM waves with high spatial frequency propagating in sGRIN are transformed into EM waves with low spatial frequency propagating in air, which contributes to diffraction-limited far-field radiation, as shown in Fig. 2(c). The two main lobes with a well depth of –7 dB are clearly observed. The normalized far-field radiation patterns of two sources with distance of 0.56λ from 4 to 16 GHz are presented in Fig. 2(d). The extracted well depth shown in Fig. 2(e) reveals that two distinct main lobes with well depths below –5 dB are yielded, which means that these two-point sources are reconstructed and discernible in the far field over a wide frequency range.

3. STRUCTURAL DESIGN AND SIMULATED RESULTS

Owing to the fact that the RI distribution of the designed lens originating from the classical half-MFE (HMFE) lens is nonmagnetic, inhomogeneous, and isotropic, all dielectric nonresonant metamaterials could be applied. For this specific RI profile varying from $n_{\min} = 1.3$ at the verge to $n_{\max} = 2.6$ at the center, five kinds of low-loss dielectric materials are adopted, namely, TP-2 dielectrics with permittivity of 4, 5, 6, 7, respectively, and photocurable resin (Vero White Plus RGD835) with

permittivity 2.8. The permittivity and loss of five selected materials are invariable in the operational bandwidth. To complete the design and manufacturing of the RI profile, a stepped RI profile is utilized to fit the curve of the ideal one, as shown in blue line in Fig. 3(a). The lens is divided into 53 layers. In line with these five dielectric materials, the designed lens is constituted of five regions depicted in the lower inset in Fig. 3(a). The outer region marked as region 1 comprises gradient inversed Y-shaped unit cells and spatially drilled air holes with gradient diameters. Four inner regions all consist of spatially drilled air holes with gradient diameters. The effective RI for the above unit cells is derived by effective medium theory and the S-parameter retrieval method. By adjusting the widths of the inversed Y-shaped unit cells and varying the diameters of drilled air holes, the stepped RI profile can be implemented. Figure 3(b) is the associated computer aided design (CAD) drawing of sGRIN.

To demonstrate the effectiveness of our designed unit cells, the subdiffraction focusing and diffraction-limited far-field radiation pattern of the designed lens with a discrete RI distribution are simulated. For the subdiffraction focusing performance, the map of the near-field electric intensity profile at the focusing line with respect to the frequency range from 4 to 20 GHz is given in Fig. 3(c). The focusing band becomes narrower and narrower with the frequency increasing. In line with the FWHM tendency in Fig. 3(d), it is found that the FWHM of designed structure varies from 0.28λ to 0.30λ, which agrees well with that of the theoretical one in overall trend. Accordingly, the focusing efficiency at the focusing line presented in Fig. 3(e) of the designed structure is higher than that of the theoretical one (nearly all above 98% numerically for this designed structure). It is validated that our design strategy is effective and practical.

The far-field radiation pattern of the designed lens is investigated by analyzing its well depth. Figure 3(f) presents the map of the normalized far-field radiation intensity profile fed by two sources with a distance of 0.56λ from 4 to 16 GHz. Two main beams in the far field are clearly observed when the lens is fed by the two sources. The extracted well depth of the far-field radiation pattern fed by two sources is exhibited in Fig. 3(g). The dashed blue line represents the well depth's theoretical values. Except for the frequency above 12 GHz, the well depth of the numerical one is deeper than that of the theoretical one in general trend, which are all below −8 dB. It is clear that the discrete lens' performance is consistent with that of the original design with continuous RI distribution.

The designed discrete subdiffraction focusing lens is manufactured by computer numerical control (CNC) machining technology and 3D printing technology.

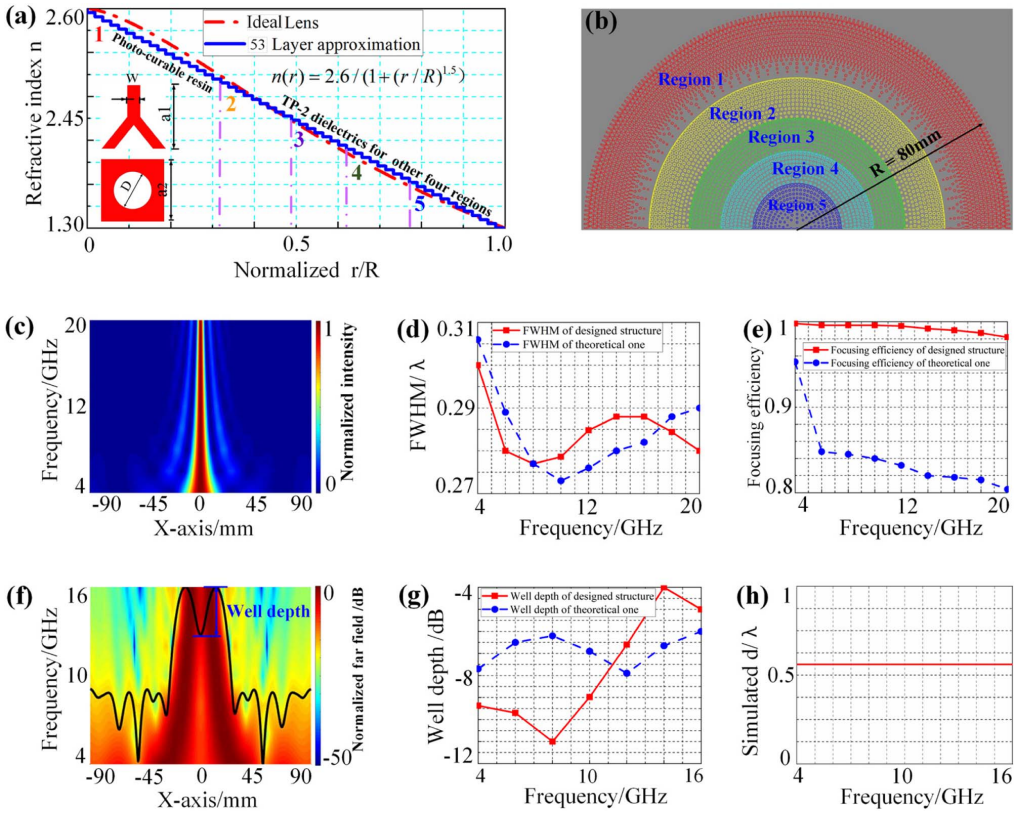

Fig. 3. Design and simulated results of sGRIN. (a) RI profile of sGRIN (dotted red line) and the discrete (solid blue line) one. The inset depicts three kinds of unit cells adopted based on the three regions in sGRIN. (b) Schematic of sGRIN; (c) map of simulated near-field intensity profile at the focusing line from 4 to 20 GHz; comparison between simulated (d) FWHM and (e) focusing efficiency of sGRIN with a discrete RI distribution (red solid line) and that of the original sGRIN with a continuous RI distribution (blue dashed line); (f) map of simulated normalized far-field intensity profile; (g) related well depth; distance between two feeding sources.

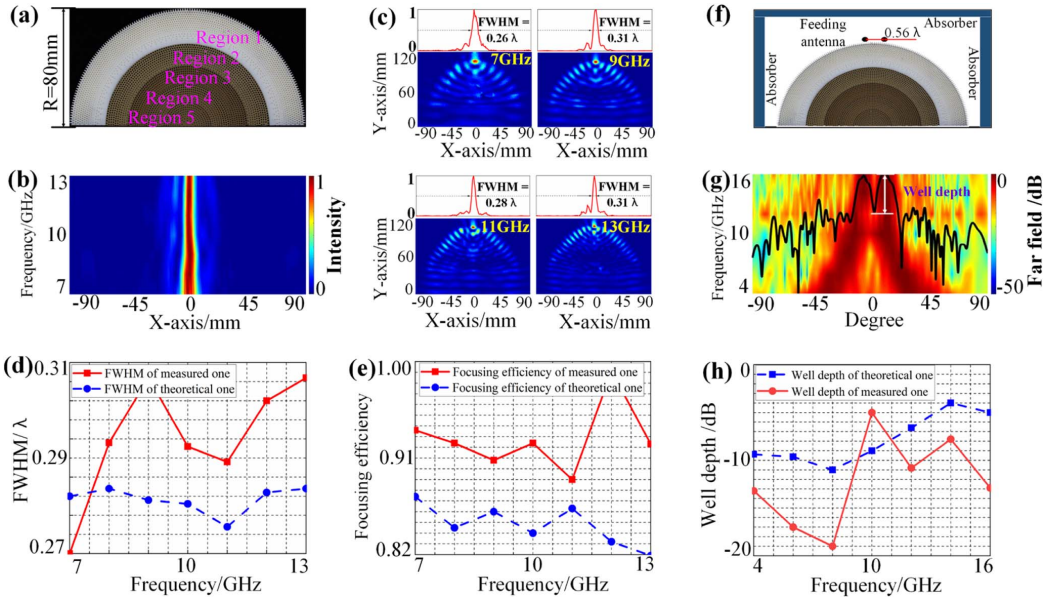

Fig. 4. Experimental results of subdiffraction focusing and diffraction-limited far-field radiation. (a) Photograph of the fabricated sample; (b) experimental map of near-field intensity profile at the focusing line from 7 to 13 GHz; (c) measured electric near-field intensity distribution and the corresponding FWHM of the combined lenses; comparison between the experimental (d) FWHM and (e) focusing efficiency of sGRIN (red solid line) with calculated results of sGRIN with a continuous RI distribution (dashed blue line); (f) schematic of the lens antenna; (g) map of measured far-field radiation intensity profiles fed by two sources with a subwavelength distance 0.56λ; (h) comparison between the measured well depths and the calculated results of sGRIN with a continuous RI distribution.

4. EXPERIMENTAL RESULTS AND DISCUSSION

Figure 4(a) is the photograph of the fabricated sample. Both the near-field electric distribution and the far-field radiation pattern are measured to validate the function of subdiffraction focusing and diffraction-limited far-field radiation. The scanning system proposed in Ref. [57] is applied to test the near-field electric distribution. An incident plane wave passing through the sample converges at the vertex of the lens, and a trenchant focus is yielded. Figures 4(b) and 4(c) describe the map of electric intensity distribution at the focusing line and related near-field electric intensity profile with plane wave illuminating the lens from 7 to 13 GHz. Besides a tiny focal spot emerging at the peak of the sample, a notable cylindrical wavefront is also generated inside the lens. The upper inset drawings in Fig. 4(c) present the FWHM along the x axis at the focus point. The FWHMs are all around 0.28λ with near-zero sidelobes, which is consistent with the narrow electric intensity focusing band. The calculated focusing efficiency of the discrete lens derived from experimental data is plotted in Fig. 4(e). The measured focusing efficiencies at the focusing line are all above 89% and vary between 89% and 99%. Given the test error, the FWHM and focusing efficiency of measured results are very consistent with the calculated results of the sGRIN with a continuous RI distribution (dashed blue line).

The sample is tested in a full anechoic chamber to get the diffraction-limited far-field radiation pattern. The sketch map of the lens antenna fed by two sources is depicted in Fig. 4(f). The experimental map of the normalized far-field radiation intensity profile fed by two sources is depicted in Fig. 4(g). Two main beams are clearly observed, and the related well depths are demonstrated in Fig. 4(h). The well depths are all below −5 dB and range from −5 to −19 dB from 4 to 16 GHz. The measured results are in good agreement with the calculated one of the sGRIN with a continuous RI distribution (dashed blue line), indicating the accuracy and practicability of the fabrication method and the discrete design methodology.

Figure 5 displays the comparison of half of the light cone angle, operational bandwidth, and focusing efficiency among SIL, negative refractive lens (NRI), SOL, hyperlens (HPL), and our designed sGRIN, respectively. It is clear that our designed lens demonstrates the best overall performance in the field of subdiffraction lenses. Generally speaking, an achromatic subdiffraction sGRIN is realized with the proposed design method. It is shown that the designed discrete lens' performance in both near field and far field agrees well with the

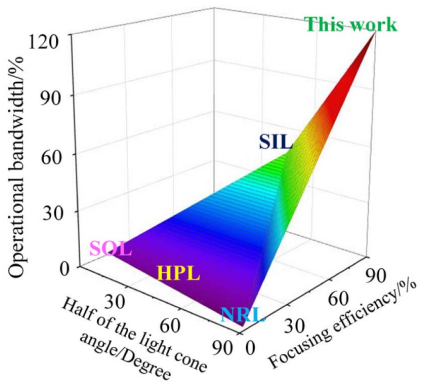

Fig. 5. Comparison of half of the light cone angle, operational bandwidth, and focusing efficiency among SIL, NRL, SOL, HPL, and our designed sGRIN.

theoretical prediction, which means that the proposed sGRIN has great potential to be used in subdiffraction imaging systems in the future.

5. DISCUSSIONS AND OUTLOOK

In summary, a semicircular all-dielectric GRIN lens with a slightly modified RI distribution of classical half-MFE lens is designed to achieve achromatic subdiffraction focusing with the FWHM around 0.28λ from 4 to 20 GHz and diffraction-limited far-field radiation from 4 to 16 GHz. Evanescent waves triggered at the upper lens/air interface lead to achromatic subdiffraction focusing. For two-point sources with a subwavelength distance of 0.56λ located at the focusing spot, the EM waves with high spatial frequency experience strong interaction in sGRIN by gradient periodic modulation and are effectively converted into EM waves with low spatial frequency, showing that diffraction-limited far-field radiation could be generated. Measured results of the near field and far field demonstrate the achromatic subdiffraction focusing and broadband diffraction-limited far-field radiation, as expected. In addition, because our proposed lens is composed of low-loss dielectric materials, this all-dielectric lens could be extended to a 3D version in the future and is of significant importance in subdiffraction imaging. The key challenge is to design and manufacture the 3D lens through just one material by 3D printed technology. Only in this way can the manufactured lens be practically feasible. But the material that could meet the demand of 3D printing and satisfy the requirement of the RI profile of our designed 3D lens simultaneously is very hard to find. Based on the current nanotechnology, the proposed method could be applied to near-infrared and visible wavebands.

Funding. National Key Research and Development Program of China (2017YFA0303702); National Natural Science Foundation of China (11634005, 11872113, 11974176, 61671314).

Acknowledgment. We thank Tianyu Dong for helpful discussions and Wei Li for help with the lens antenna setup.

Disclosures. The authors declare no conflicts of interest.

Data Availability. Data used to support the findings of this study are included within the paper.

REFERENCES

1. E. Abbe, "Resolution of microscopes," Arch. Mikrosk. Anat **9**, 413–468 (1873).
2. J. B. Pendry, "Negative refraction makes a perfect lens," Phys. Rev. Lett. **85**, 3966–3969 (2000).
3. N. Fang, H. Lee, C. Sun, and X. Zhang, "Negative refraction makes a perfect lens," Science **308**, 534–537 (2005).
4. T. Taubner, D. Korobkin, Y. Urzhumov, G. Shvets, and R. Hillenbrand, "Near-field microscopy through a SiC superlens," Science **313**, 1595 (2006).
5. E. Cubukcu, K. Aydin, E. Ozbay, S. Foteinopoulou, and C. M. Soukoulis, "Subwavelength resolution in a two-dimensional photonic-crystal-based superlens," Phys. Rev. Lett. **91**, 207401 (2003).
6. K. Aydin, I. Bulu, and E. Ozbay, "Subwavelength resolution with a negative-index metamaterial superlens," Appl. Phys. Lett. **90**, 254102 (2007).
7. W. Cai, D. A. Genov, and V. M. Shalaev, "Superlens based on metal-dielectric composites," Phys. Rev. B **72**, 193101 (2005).
8. V. A. Podolskiy and E. E. Narimanov, "Near-sighted superlens," Opt. Lett **30**, 75–77 (2005).
9. A. Salandrino and N. Engheta, "Far-field subdiffraction optical microscopy using metamaterial crystals: theory and simulations," Phys. Rev. B **74**, 075103 (2006).
10. Z. Jacob, L. V. Alekseyev, and E. Narmanov, "Optical hyperlenses: far-field imaging beyond the diffraction limit," Opt. Express **14**, 8247–8256 (2006).
11. Z. W. Liu, H. Lee, Y. Xiong, C. Sun, and X. Zhang, "Far-field optical hyperlens magnifying sub-diffraction-limited objects," Science **315**, 1686 (2007).
12. J. B. Sun, M. I. Shalaev, and N. M. Litchinitser, "Experimental demonstration of a non-resonant hyperlens in the visible spectral range," Nat. Commun **6**, 7201 (2015).
13. J. Rho, Z. Ye, Y. Xiong, X. Yin, Z. W. Liu, H. Choi, G. Bartal, and X. Zhang, "Spherical hyperlens for two-dimensional sub-diffractional imaging at visible frequencies," Nat. Commun. **1**, 143 (2010).
14. D. Z. Albert, L. Vaidman, and Y. Aharonov, "How the result of a measurement of a component of the spin of a spin-1/2 particle can turn out to be 100," Phys. Rev. Lett. **60**, 1351–1354 (1988).
15. M. V. Berry, "Evanescent and real waves in quantum billiards and Gaussian beams," J. Phys. A **27**, L391–L398 (1994).
16. M. V. Berry and S. Popescu, "Evolution of quantum superoscillations and optical super resolution without evanescent waves," J. Phys. A **39**, 6965–6977 (2006).
17. K. Huang, H. P. Ye, J. H. Teng, S. P. Yeo, B. Luk'yanchuk, and C.-W. Qiu, "Optimization-free superoscillatory lens using phase and amplitude masks," Laser Photon. Rev. **8**, 152–157 (2014).
18. E. T. F. Rogers, J. Lindberg, T. Roy, S. Savo, J. E. Chad, M. R. Dennis, and N. I. Zheludev, "A super-oscillatory lens optical microscope for subwavelength imaging," Nat. Mater. **11**, 432–435 (2012).
19. K. S. Rogers, E. T. F. Rogers, N. I. Zheludev, and G. Yuan, "Far-field superoscillatory metamaterial superlens," Phys. Rev. Appl. **11**, 024073 (2019).
20. Q. Zhang, F. Dong, H. Li, Z. Wang, G. Liang, Z. Zhang, Z. Wen, Z. Shang, G. Chen, L. Dai, and W. Chu, "High-numerical-aperture dielectric metalens for super-resolution focusing of oblique incident light," Adv. Opt. Mater. **8**, 1901885 (2020).
21. R. Zuo, W. Liu, H. Cheng, S. Chen, and J. Tian, "Breaking the diffraction limit with radially polarized light based on dielectric metalenses," Adv. Opt. Mater. **6**, 1800795 (2018).
22. L. Chen, J. Liu, X. Zhang, and D. Tang, "Achromatic super-oscillatory metasurface through optimized multiwavelength functions for subdiffraction focusing," Opt. Lett. **45**, 5772–5775 (2020).
23. Z. Wu, F. Dong, S. Zhang, S. Yan, G. Liang, Z. Zhang, Z. Wen, G. Chen, L. Dai, and W. Chu, "Broadband dielectric metalens for polarization manipulating and superoscillation focusing of visible light," ACS Photon. **7**, 180–189 (2020).
24. D. Tang, C. Wang, Z. Zhao, Y. Wang, M. Pu, X. Li, P. Gao, and X. Luo, "Ultrabroadband superoscillatory lens composed by plasmonic metasurfaces for sub-diffraction light focusing," Laser Photon. Rev. **9**, 713–719 (2015).
25. D. Tang, L. Chen, and J. Liu, "Visible achromatic super-oscillatory metasurfaces for sub-diffraction focusing," Opt. Express **27**, 12308–12316 (2019).
26. E. T. Rogers and N. I. Zheludev, "Optical super-oscillations: sub-wavelength light focusing and super-resolution imaging," J. Opt. **15**, 094008 (2013).
27. F. Qin, K. Huang, J. Wu, J. Teng, C.-W. Qiu, and M. Hong, "A supercritical lens optical label-free microscopy: sub-diffraction resolution and ultra-long working distance," Adv. Mater. **29**, 1602721 (2017).
28. C. L. Hao, Z. Q. Nie, H. P. Ye, H. Li, Y. Luo, R. Feng, X. Yu, F. Wen, Y. Zhang, C. Y. Yu, J. H. Teng, B. Luk'yanchuk, and C.-W. Qiu, "Three-dimensional supercritical resolved light-induced magnetic holography," Sci. Adv. **3**, e1701398 (2017).

29. K. Huang, H. Liu, F. J. Garcia-Vidal, M. H. Hong, B. Luk'yanchuk, J. H. Teng, and C.-W. Qiu, "Ultrahigh-capacity non-periodic photon sieves operating in visible light," Nat. Commun. **6**, 7059 (2015).
30. X. Lu, Y. Guo, M. Pu, Y. Zhang, Z. Li, X. Ma, and X. Luo, "Broadband achromatic metasurfaces for sub-diffraction focusing in the visible," Opt. Express **29**, 5947–5958 (2021).
31. Y. J. Bao, J. C. Ni, and C.-W. Qiu, "A minimalist single-layer metasurface for arbitrary and full control of vector vortex beams," Adv. Mater. **32**, 1905659 (2020).
32. S. Chen, Z. Li, W. Liu, H. Cheng, and J. Tian, "From single-dimensional to multidimensional manipulation of optical waves with metasurfaces," Adv. Mater. **31**, 1802458 (2019).
33. S. Chen, W. W. Liu, Z. C. Li, H. Cheng, and J. G. Tian, "Metasurface-empowered optical multiplexing and multifunction," Adv. Mater. **32**, 2070022 (2020).
34. S. Wang, P. C. Wu, V. C. Su, Y. C. Lai, M. K. Chen, H. Y. Kuo, B. H. Chen, Y. H. Chen, T. T. Huang, and J. H. Wang, "A broadband achromatic metalens in the visible," Nat. Nanotechnol **13**, 227–232 (2018).
35. A. Ndao, L. Y. Hsu, J. Ha, J.-H. Park, C. Chang-Hasnain, and B. Kante, "Octave bandwidth photonic fishnet-achromatic-metalens," Nat. Commun. **11**, 3205 (2020).
36. X. Luo, D. Tsai, M. Gu, and M. Hong, "Extraordinary optical fields in nanostructures: from sub-diffraction-limited optics to sensing and energy conversion," Chem. Soc. Rev. **48**, 2494–2548 (2019).
37. S. Shrestha, A. C. Overvig, M. Lu, A. Stein, and N. Yu, "Broadband achromatic dielectric metalenses," Light Sci. Appl. **7**, 85 (2018).
38. S. Wang, P. C. Wu, V. C. Su, Y. C. Lai, C. H. Chu, J. W. Chen, S. H. Lu, J. Chen, B. Xu, and C. H. Kuan, "Broadband achromatic optical metasurface devices," Nat. Commun. **8**, 187 (2017).
39. S. M. Mansfield and G. S. Kino, "Solid immersion microscope," Appl. Phys. Lett. **57**, 2615–2616 (1990).
40. A. Bogucki, L. Zinkiewiz, M. Grzeszczyk, W. Pacuski, K. Nogajewski, T. Kazimierczuk, A. Rodek, J. Suffczynski, K. Watanabe, T. Taniguchi, P. Wasylczyk, M. Potemski, and P. Kossacki, "Ultra-long-working-distance spectroscopy of single nanostructures with aspherical solid immersion microlenses," Light Sci. Appl. **9**, 48 (2020).
41. M.-S. Kim, T. Scharf, M. T. Haq, W. Nakagawa, and H. P. Herzig, "Subwavelength-size solid immersion lens," Opt. Lett. **36**, 3930–3932 (2011).
42. J. Chen, X. Yuan, M. Chen, X. Cheng, A. Zhang, G. Peng, W. L. Song, and D. Fang, "Ultrabroadband three-dimensional printed radial perfectly symmetric gradient honeycomb all-dielectric dual-directional lightweight planar Luneburg lens," ACS Appl. Mater. Interfaces **10**, 38404–38409 (2018).
43. J. Chen, Y. Lin, G. Peng, Y. Huang, A. Zhang, W. L. Song, M. Chen, Z. Liu, and D. Fang, "An all-dielectric 3D Luneburg lens constructed by common-vertex coaxial circular cones," J. Phys. D **53**, 015110 (2020).
44. J. Chen, H. Chu, Y. Zhang, Y. Lai, M. Chen, and D. Fang, "Modified Luneburg lens for achromatic sub-diffraction focusing and directional emission," IEEE Trans. Antennas Propag., https://dx.doi.org/10.1109/TAP.2021.3083843 (2021).
45. J. Chen, H. Chu, Y. Huang, Y. Lai, M. Chen, Z. Liu, and D. Fang, "Ultrabroadband compact lens antenna with high performance based on a transmission gradient index medium," J. Phys. D **54**, 175101 (2020).
46. J. Chen, H. Chu, Y. Lai, Z. Liu, H. Chen, M. Chen, and D. Fang, "Conformally mapped Mikaelian lens for broadband achromatic high resolution focusing," Laser Photon. Rev. **15**, 2000564 (2021).
47. C. Guo, T. Urner, and S. Jia, "3D light-field endoscopic imaging using a GRIN lens array," Appl. Phys. Lett. **116**, 101105 (2020).
48. M. G. Scopelliti and M. Chamanzar, "Ultrasonically sculpted virtual relay lens for *in situ* microimaging," Light Sci. Appl. **8**, 65 (2019).
49. J. Nagar, S. D. Campbell, and D. H. Werner, "Apochromatic singlets enabled by metasurface-augmented GRIN lenses," Optica **5**, 99–102 (2018).
50. W. Jiang, C.-W. Qiu, T. Han, Q. Cheng, H. Ma, S. Zhang, and T. Cui, "Broadband all-dielectric magnifying lens for far-field high-resolution imaging," Adv. Mater. **25**, 6963–6968 (2013).
51. W. Jiang, S. Ge, T. Han, S. Zhang, M. Mehmood, C.-W. Qiu, and T. Cui, "Shaping 3D path of electromagnetic waves using gradient-refractive-index metamaterials," Adv. Sci. **3**, 1600022 (2016).
52. N. Zhang, W. X. Jiang, H. F. Ma, W. X. Tang, and T. J. Cui, "Compact high-performance lens antenna based on impedance-matching gradient-index metamaterials," IEEE. Trans. Antennas. Propag. **67**, 1323–1328 (2018).
53. A. Forbes, "Common elements for uncommon light: vector beams with GRIN lenses," Light Sci. Appl. **8**, 111 (2019).
54. O. Bitton, R. Bruch, and U. Leonhardt, "Two-dimensional Maxwell fisheye for integrated optics," Phys. Rev. Appl. **10**, 044059 (2018).
55. A. Arbabi, Y. Horie, A. J. Ball, M. Bagheri, and A. Faraon, "Subwavelength-thick lenses with high numerical apertures and large efficiency based on high-contrast transmitarrays," Nat. Commun. **6**, 7069 (2013).
56. R. J. Potton, "Reciprocity in optics," Rep. Prog. Phys. **67**, 717–754 (2004).
57. D. Schurig, J. J. Mock, B. J. Justice, S. A. Cummer, J. B. Pendry, A. F. Starr, and D. R. Smith, "Metamaterial electromagnetic cloak at microwave frequencies," Science **314**, 977–980 (2006).